Energy materials

Room temperature manufacture of dense NaSICON solid electrolyte films for all-solid-state-sodium batteries

Mutlucan Sozak[1,*] , Tobias Nazarenus[1], Jörg Exner[1], Jaroslaw Kita[1], and Ralf Moos[1]

[1] *Department of Functional Materials, University of Bayreuth, Universitätsstraße 30, 95447 Bayreuth, Germany*

ABSTRACT

Sodium (*Na*) Super-*I*onic *CON*ductor (NaSICON) solid electrolyte (SE) powders ($Na_3Zr_2Si_2PO_4$) were prepared by the mixed oxide technique using a planetary ball mill and synthesized via solid-state method at temperatures ranging from 950 to 1200 °C. The powders with 95% pure NaSICON phase were deposited on different substrates via Powder Aerosol Deposition (PAD) at room temperature directly from the powders and fully dense ceramic films were obtained. X-ray diffractometry including Rietveld refinement were carried out on both the calcined powders and the resulting films to determine the crystallographic properties. Subsequently, the electrical properties of the resulting films were characterized and the effect of annealing at temperatures between 100 and 600 °C on the ionic conductivity of NaSICON PAD films was evaluated. Annealed films were measured in the temperature range 50 and 250 °C to calculate the activation energy E_a of the PAD films. Our work demonstrates a successful room temperature deposition of dense NaSICON electrolyte films on different substrates, which is promising for stationary energy storage applications of solid-state-sodium batteries.

Introduction

Li-ion batteries have been widely studied by researchers worldwide, and the technology is about to reach its limits in terms of specific capacity [1, 2]. Additionally, safety concerns remain from past to today due to liquid electrolyte components. In the past decade, one research focus is on all-solid-state batteries (ASSB) with nonflammable solid electrolytes. Due to the huge abundance of the element "sodium" in the earth crust, some researchers consider that Na-ion batteries would open a new era of batteries in terms of their abundancy, sustainability, and lower-cost [3].

Handling Editor: Till Froemling.

Address correspondence to E-mail: functional.materials@uni-bayreuth.de

Sodium (*Na*) *S*uper-*I*onic *CON*ductor (NaSICON) solid-state ionic conductors were introduced before the emergence of Li-ion batteries [4]. Hong et al. [5] first prepared NaSICON type Na-ion solid electrolytes in 1976 and demonstrated their ionic conductivity. From that time forth, comprehensive studies have been published covering its use for gas sensors, ion-selective sensors, or sodium all-solid-state batteries (ASSB) [6].

Several production techniques have been reported to build up solid electrolytes (SE) in ASSBs; however, very few of those methods were successful to provide thin solid electrolyte films with thicknesses in the 20–50 μm range. Thicker SE components come along with higher electrical resistances. On the other hand, the methods reported so far to implement SEs require high sintering temperatures above 1000 °C, which may lead to very high production costs. The powder aerosol deposition (PAD) method, also known as aerosol deposition method (ADM) [7], vacuum cold spray [8], or vacuum kinetic spray [9], may help to overcome the difficulties of realizing membranes in the desired thickness range and reduce costs by excluding the additional high-temperature sintering step. The fundamental principle of the method is based on the mechanism of room temperature impact consolidation (RTIC) [10], where particles collide with the substrate at high velocity, and during this collision, a portion of the kinetic energy of the particles is converted into bonding energy and dense ceramic films are formed.

A variety of ceramic materials, e.g., Al_2O_3 [10–14], YSZ [15–19], ZrO_2 [20], LLZO ($Li_7La_3Zr_2O_{12}$) [21, 22], LLZTO ($Li_6La_3Zr_2TaO_{12}$) [23], LAGP ($Li_{1.5}Al_{0.5}Ge_{1.5}P_3O_{12}$) [24], LATP ($Li_{1+x}Al_xTi_{2-x}P_3O_{12}$) [25], BFT ($BaFe_{0.7}Ta_{0.3}O_{3-\delta}$) [26, 27], $BaTiO_3$ [28–32], and many more compounds can be deposited by PAD on a wide range of substrate materials, with the intention to manufacture functional films that are used as solid electrolytes, proton conductors, insulators, or sensors. Powder aerosol deposition of $Na_3V_2(PO_4)_3$ electrode material has been reported in [33]; however, a detailed study on the electrical properties of PAD-deposited NaSICON solid electrolyte for ASSB has not been reported yet.

In this work, we investigated the film deposition of NaSICON material and carried out first measurements of the electrical properties of thick NaSICON films. We produced NaSICON powders and analyzed resulting powders regarding their morphological and structural properties. Then, we deposited thick films from the powders on different substrates, characterized the films and investigated the effects of post-heat-treatment processes on the conductivity of NaSICON PAD films. The main steps of the study are depicted in Fig. 1, namely powder preparation, film production, and characterization of functional NaSICON films.

Experimental

Powder synthesis

NaSICON ($Na_3Zr_2Si_2PO_4$) solid electrolyte powders were synthesized via a solid-state synthesis route (mixed-oxide route). The starting raw materials of Na_2CO_3 ($\geq$ 99%, Sigma Ald.), $NH_4H_2PO_4$ ($\geq$ 99.5%, Sigma Ald.), ZrO_2 (99%, Sigma Ald.), and SiO_2 (99.5%, Alfa Aesar) were weighed-in according to the stoichiometric ratio of $Na_3Zr_2Si_2PO_4$ and homogenized for 15 min at 400 rpm in a planetary ball mill (Fritsch Pulverisette 5, Idar-Oberstein). Mixing was carried out in a zirconia jar (stabilized with 3.5 wt% MgO) with zirconia balls (stabilized with 5 mol% Y_2O_3; Ø10 mm). The ball-to-powder weight ratio was 3:1, respectively. Cyclohexane was used as milling medium. Afterward, cyclohexane was evaporated in a fume hood and the powder mixtures were calcined in air for 5 h between 950 and 1200 °C in 50 °C steps in an aluminum oxide crucible covered with a platinum foil (5 K min^{-1} heating and cooling rate).

To obtain a suitable particle size distribution for the powder aerosol deposition process, calcined powders were grinded again by using the same grinding jars and media, this time for 35 min (400 rpm, ball-to-powder ratio 3:1). Then, cyclohexane was evaporated by a rotary evaporator (Heidolph Hei-VAP Advantage, Schwabach, Germany) and powders were kept in a drying-oven at 120 °C for 24 h. In order to avoid large agglomerates, powders were sieved through 90 μm mesh sized screen. Finally, these powders were stored in a furnace operating at 200 °C to obtain dry, free-flowing powder prior to spraying process.

Powder aerosol deposition

Thick films were fabricated via a custom-made PAD device. The setup in our laboratory and its fundamentals were reported elsewhere [34]. Powders were
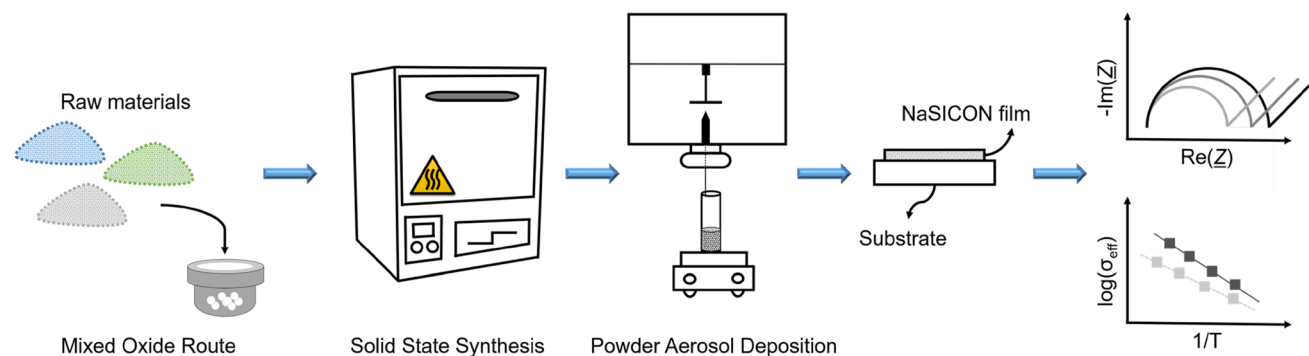
Figure 1 Flowchart of the main processes.

sprayed on two different substrates; stainless steel (20 mm × 20 mm × 2 mm), and alumina with screen-printed interdigital electrodes (IDEs). Detailed information on interdigital electrodes and their properties can be found in [18, 35]. As carrier gas, oxygen was used with a flow rate of 8 L min^{-1}. The resulting pressure inside the aerosol generator was 25 kPa and the pressure within the deposition chamber was 0.5 kPa. The powders in the aerosol were accelerated toward the deposition chamber, passing through a converging slit nozzle with an orifice of 10 × 0.5 mm^2, by utilizing the pressure difference between aerosol chamber and aerosol generator. The distance between the converging nozzle and the substrates was adjusted to 3 mm. The stage (where the substrates were attached) was moved horizontally at a speed of 5 mm s^{-1} over 80 scans to obtain 10 mm × 10 mm areal films.

Characterization methods

Before the deposition, the particle sizes of the powders were measured by laser scattering (Mastersizer 2000, Malvern Instruments Ltd, Malvern, UK). Phase compositions of powders and films were determined by X-ray diffractometry (XRD, D8-Advance, Bruker, diffractometer with Ge-K$_{\alpha 1}$ monochromator—1.5406 Å and energy-dispersive 1-D LYNXEYE detector). Powders were subjected to X-rays between 10° and 80° (2θ) in 0.02° steps for 0.2 s holding time and the XRD parameters on the films were determined between 10° and 55° in steps of 0.01° for 0.5 s exposure time. The diffraction data were analyzed using the search and match feature in *X'Pert High-Score Plus* software combined with ICDD PDF-4 + database (2020) to evaluate the crystal structure. The crystallite size and the internal strain were

estimated by fitting the data using pseudo-Voigt functions for Rietveld refinement in TOPAS-Academic Software. Details of the refinement process are provided in the supplementary information.

The thicknesses of the PAD films were measured by a stylus profilometer (PGK/S″, Mahr, Göttingen, Germany). The microstructures of the sprayed films were examined by scanning electron microscopy (SEM, Leo 1530 VP, Zeiss, Oberkochen, Germany) on its cross section. To prepare samples for SEM, the films sprayed on stainless steel substrates were embedded in resin and then cut in half. Subsequently, the surfaces were grinded and polished.

The electrical conductivity of the as-deposited NaSICON films was determined by two-wire electrochemical impedance spectroscopy (EIS) on IDE samples from room temperature up to 600 °C in 100 °C steps. The samples were heated at a rate of 5 K min^{-1} in an alumina tube furnace, and the impedance was measured at the end of 20 min of dwell time for each temperature step by a precision impedance analyzer (Novocontrol Alpha-A, Germany) in a frequency range from 1 MHz to 1 Hz at 150 mV rms amplitude of the AC signal. EIS data were fitted in *Relaxis3* software. As an equivalent circuit, we used parallel elements of a resistor (R) and a constant phase element (CPE) and another CPE element in series to describe the Na$^+$ ion blocking effect of the platinum electrodes (R||CPE)-(CPE).

The effective conductivity σ_{eff} is calculated by Eq. 1 [18, 36, 37]. In Eq. 1, R_{tot} denotes the total resistance and t the film thickness. The IDE geometry is determined by the finger length l = 4.5 mm, the finger width w = 100 μm, the spacing between each fingers d = 100 μm, and the number of fingers n = 15.

$$\sigma_{\text{eff}} = \frac{d}{R_{\text{tot}} \cdot A} = \frac{d}{R_{\text{tot}} \cdot [(2n-1) \cdot l \cdot t + 2n \cdot w \cdot t]} \quad (1)$$

Annealed IDEs were post-treated at temperatures between 50 and 250 °C to determine the activation energy E_a of the NaSICON films annealed at different temperatures. The activation energy was calculated using the slope m of the linear fitting of the Arrhenius-like plots that were created by plotting $\log \sigma_{\text{eff}}$ vs. $1000/T$ for each annealing temperature. According to Eq. 2, the activation energy can be calculated, with k_B being Boltzmann's constant:

$$\sigma_{\text{eff}} = \sigma_0 \cdot \exp\left(-\frac{E_a}{k_B T}\right) \quad (2)$$

Results and discussion

Properties of the powder used in aerosol deposition

The NaSICON powders were prepared as described above. XRD and Rietveld analyses were utilized to verify the phase content of all powders. Figure 2a shows the XRD patterns of powders calcined between 950 and 1200 °C for 5 h. The graph displays the 2θ range between 27° and 32°, where the main reflections of the monoclinic zirconia (00-037-1484) and the monoclinic NaSICON (00-035-0412) phases are located. Only the zirconia reflections occur in the sample calcined at 950 °C. Reflections from the NaSICON phase appear at 1000 °C and their intensities increase with increasing calcination temperature. Simultaneously, the intensities of reflections from zirconia decrease. Regarding to volatilization of
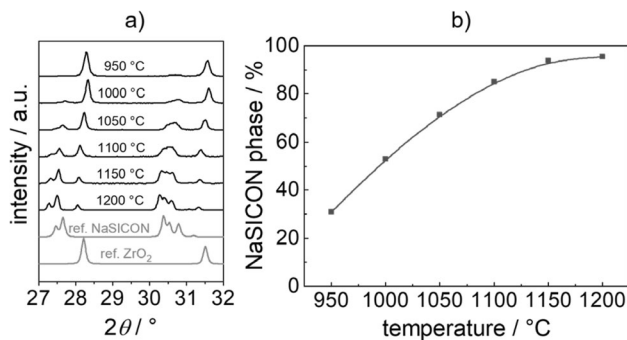
Na and P elements during calcination process [38, 39], small amounts of zirconia impurities are still present in the pattern of the sample calcined at 1200 °C. However, this pattern coincides well to the monoclinic phase of NaSICON. The amount of the NaSICON phase in each powder derived by Rietveld analysis is shown in Fig. 2b. The powder calcined at 1200 °C mainly consists of monoclinic NaSICON phase (95.4%) with only a small monoclinic ZrO_2 impurity (see Fig. S1 for the Rietveld refinement). Therefore, for the following experiments, only the powders calcined at 1200 °C were used.

The particle size distribution of NaSICON powders prepared for PAD process is shown in Fig. 3. The powder exhibits a d_{50} value of 4.8 μm. This value coincides with the upper range of suitable particle sizes (0.2–5 μm) for the PAD process [40]. It can be seen from Fig. 3 that the powder has a merged bimodal distribution with a range of 0.8 μm (d_{10}) to 13 μm (d_{90}).

The SEM image of the final powder prior to the PAD process is shown in Fig. 3b. The powder consists of bigger particles about 10–30 μm with a fraction of smaller particles in the range of 0.2–1 μm attached to the surface of the larger ones.

PAD of NaSICON

The deposition process of NaSICON powders on stainless steel and alumina (with IDE structure) substrates resulted in dense and homogeneous films. Depending on the parameter setup of the PAD process, thick films were fabricated with thicknesses between 3.5 and 10 μm. Figure 4a shows the thickness profile of a film that is recorded in spraying direction (depicted with an arrow in the image). The cross-sectional image of the substrate in Fig. 4b reveals a fully dense and crack-free NaSICON PAD film. None of the bigger particles from the starting powder is visible in the SEM image. This shows that particles were broken into small fragments to form the film. For the PAD process, this is a typical behavior of particles during film formation [41, 42].

To investigate whether changes in the crystal structure have occurred as a result of the deposition process, XRD analyses of deposited films on stainless steel substrates were carried out (see Fig. S2 for the Rietveld refinement). The recorded XRD data of the powder are compared with the PAD film in Fig. 5 including the reference patterns from the database.
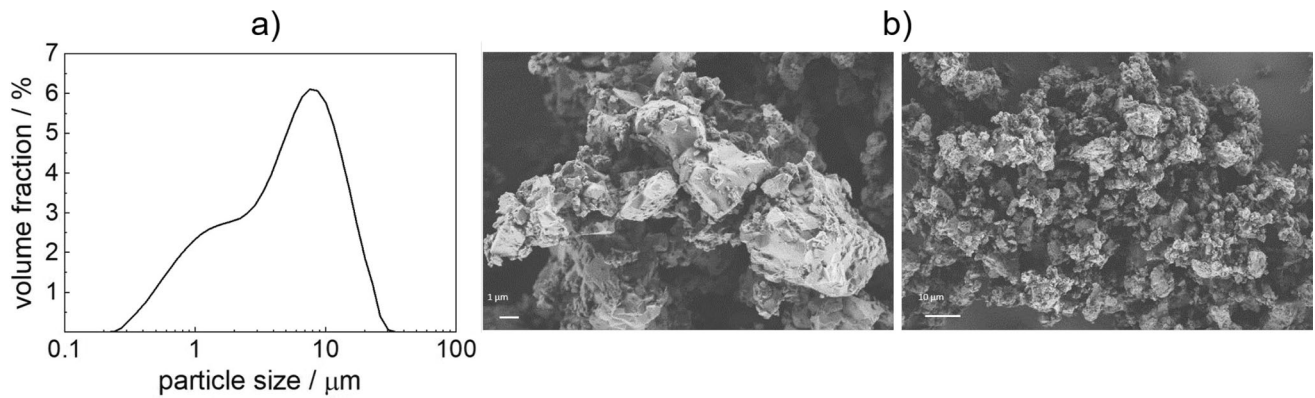

Figure 2 **a** XRD patterns of NaSICON powders calcined at 950–1200 °C. **b** Rietveld results of each powder calcined at different temperatures.

Figure 3 **a** Particle size distribution of the NaSICON powder used for the PAD process. **b** SEM images of NaSICON powder with different magnifications.
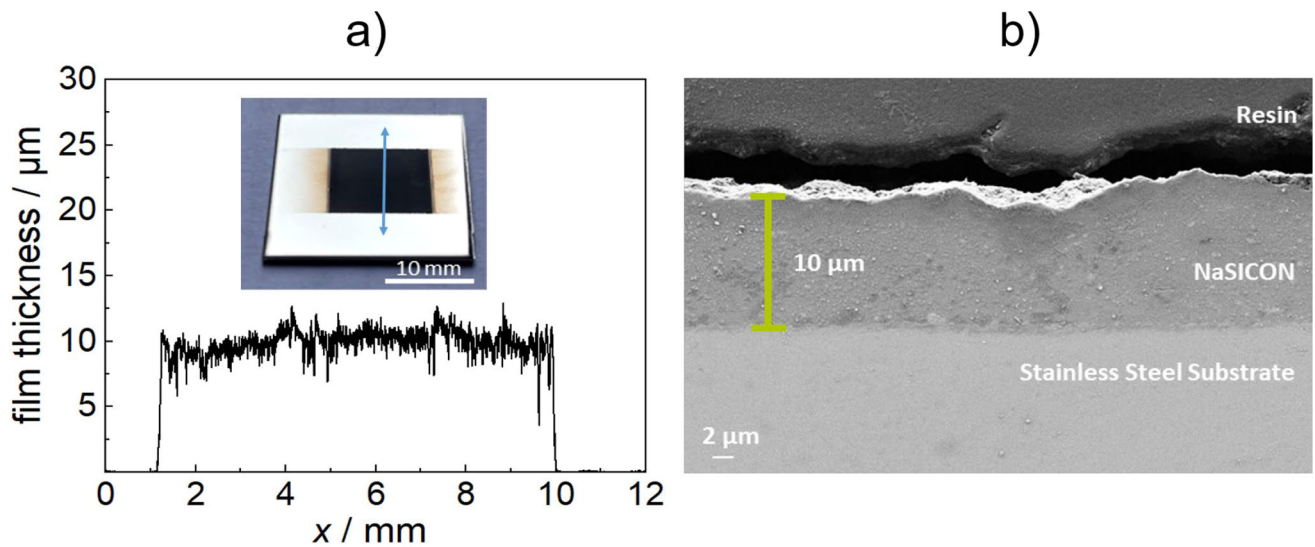

Figure 4 **a** Example for a thickness profile of a NaSICON thick film deposited on a stainless steel substrate **b** cross-sectional SEM image of the film.

The reflections from the stainless steel substrate ($\gamma(111)$, $\gamma(200)$) are visible in the measured pattern of the deposited film. The impurity reflections of ZrO_2 in the powder and deposited film are marked with filled triangles. The pattern of the deposited film matches with the simulated reference monoclinic NaSICON (00-035-0412) and the reference monoclinic ZrO_2 (00-037-1484) reflections in terms of their 2θ positions and intensities. However, the reflections are broadened due to strain and distortion of the crystallite lattice as a result of high impact energy of the particles [10]. This is an essential and well-known feature of PAD-processed ceramic films [43]. The crystallite size and microstrain values of the NaSICON film, respectively, 34 nm and 0.45% were calculated by Rietveld refinement according to data on
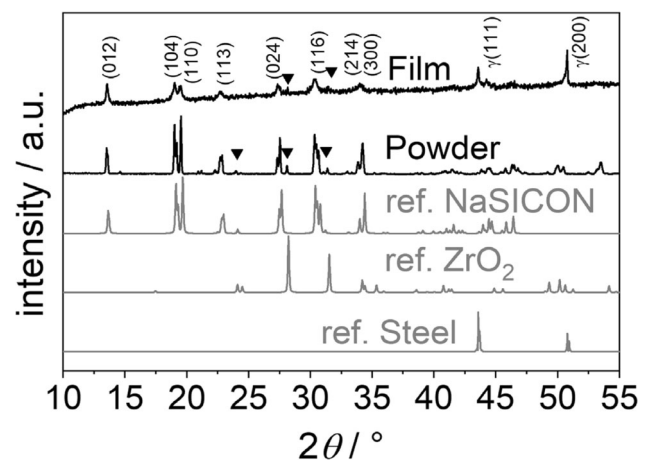

Figure 5 X-Ray diffraction of a NaSICON PAD film on stainless steel substrate.

the phase card of NaSICON. These values are in accordance with the reported data for crystallite size and microstrain of PAD films. The reported values of the crystallite size and microstrain of CeO_2 films prepared by PAD are 12–55 nm and 0.06–0.56%, respectively, depending on the powder pretreatment temperature [44] and, for PAD films of $BaZrO_3$, $BaSnO_3$, and $BaCeO_3$, the values are 14–34 nm and 0.2–0.3%, respectively [45]. Smaller crystallite sizes and increased microstrain in PAD films are expected as a result of the RTIC mechanism [44].

Electrical conductivity of NaSICON PAD films

The Nyquist plots of the impedance spectra of the IDEs annealed up to 600 °C are shown in Fig. 6a. The EIS data were recorded at the target temperature. The impedance spectra for all samples consist of one depressed semicircle starting at the origin at high frequencies, and a tail due to ion blocking at low frequencies, which indicates ion conduction in the material [46]. Therefore, the separation of grain and grain boundary contributions is not possible. With increasing temperature, semicircles become smaller and the total resistances reduce. According to Eq. 1, the effective in-plane conductivity σ_{eff} was determined as 7.1×10^{-7} S cm^{-1} at room temperature. The conductivity value increases with increasing temperature and at 200 °C, a value of 7×10^{-5} S cm^{-1} was found for NaSICON electrolyte PAD films (Fig. 6b). Compared to the high total conductivity values (10^{-4} to 10^{-3} S cm^{-1}) of bulk materials reported in the literature [5, 6, 38, 39, 47–50], PAD films of NaSICON solid electrolytes exhibit a significantly lower electrical conductivity in the as-deposited state.

It is claimed in the literature that the distorted crystallite structure due to increased strain and the distorted surfaces between the nano-grains are responsible for the lower conductivities [21, 43].

All samples that were previously annealed between room temperature and 600 °C were subsequently heated to temperatures between 50 and 250 °C and EIS data were collected in order to gather information about the activation energy E_a of the conduction processes. Arrhenius-like plots are shown in Fig. 7a. The effective total conductivity σ_{eff} of the IDEs annealed up to 600 °C (see Fig. 6) are also included in Fig. 7a for comparison and the data set were labeled as "as-deposited" because the samples on IDEs were not subjected to a pretreatment. These IDEs were heated and subsequently dwelled for 20 min at the target temperature before an EIS measurement was performed, and the IDEs were then cooled down to room temperature again.

The initially heated and then cooled IDEs were labeled as "previously annealed" in the graph. The IDE labeled as "not annealed" was only post-treated between 50 and 250 °C without previous treatment and it was compared with the previously annealed IDEs. The measured data on the graph were presented with filled symbols. The extrapolated data were shown with unfilled labels. The conductivity values of "not annealed," "previously annealed at 200 °C," and "previously annealed at 300 °C" samples coincide with the sample in the "as-deposited" state. No increase in conductivity and activation energy values were observed in the previously annealed IDEs at 20 and 300 °C (Fig. 7a). The phase transition temperature reported in the literature ranges between 130 and 300 °C (from monoclinic to rhombohedral structure) depending on the
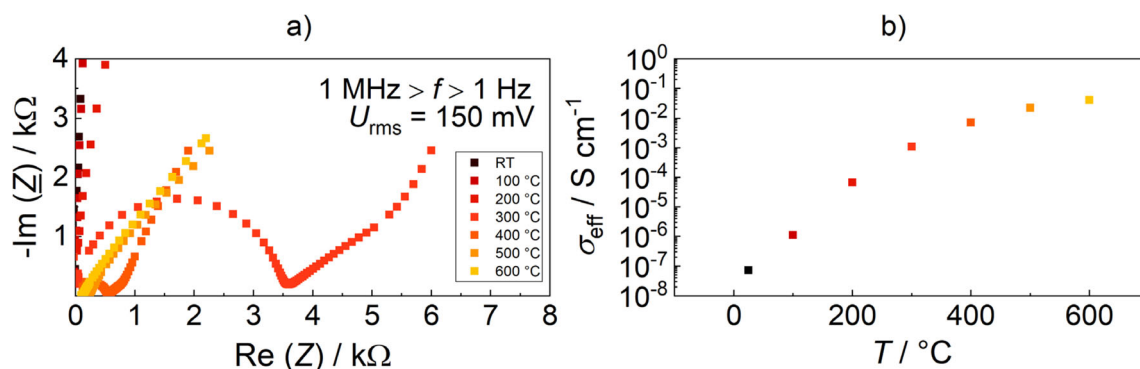

Figure 6 **a** Nyquist plots of temperature-dependent EIS measurements, **b** effective conductivity values of each sample at corresponding temperature.
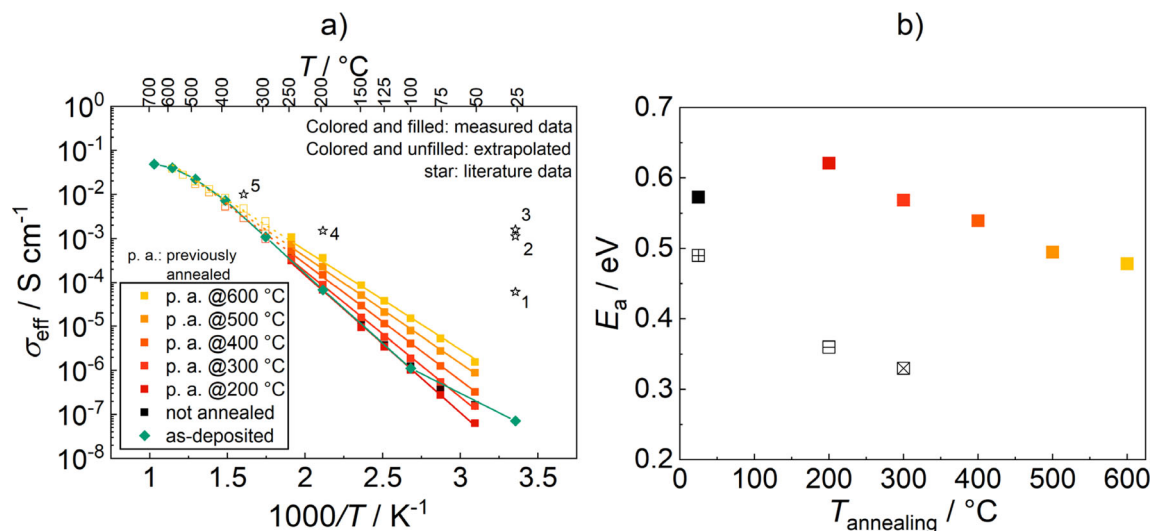
Figure 7 a Arrhenius-like representation of the effective conductivity. While the colored and filled squares indicate the measurement points, the unfilled ones represents the extrapolated data. The literature data are labeled as stars for comparison ☆^{1} and ☆^{5} [47], ☆^{4} [6], ☆^{3} [38], ☆^{2} [39]. **b** Activation energy for the samples post-treated at different temperatures (literature data: ⊞ [49], ⊟ [50], ⊠ [51]).

composition of NaSICON [52]. The monoclinic structure has one more Na site for the occupation of Na^+ ions, which leads to additional conduction pathways that makes the monoclinic structure more conductive than the rhombohedral structure [53]. The phase transition from highly conductive monoclinic phase to rhombohedral structure, where sodium ions are less mobile, may explain the increase in activation energy of previously annealed IDEs at 200 and 300 °C. The IDEs annealed above 300 °C, however, exhibit an increased conductivity. The graph shows that the initially low conductivity values at room temperature and up to 300 °C are permanently increased, e.g., the conductivity of the sample annealed at 600 °C increases by one orders of magnitude at 50 °C compared to the value of the as-deposited sample (from 1.6×10^{-7} S cm^{-1} to 1.5×10^{-6} S cm^{-1}). The effective conductivity values of similar compositions reported in the literature are also included in Fig. 7a. Compared to conductivity values of bulk NaSICON SEs at room temperature reported by Naqash et al. [38] and Narayanan et al. [39], 1.6×10^{-3} S cm^{-1} and 1.13×10^{-3} S cm^{-1}, respectively, the PAD-deposited NaSICON films exhibit a lower conductivity at room temperature, even when annealed at 600 °C (1.5×10^{-6} S cm^{-1}). However, Lalère et al. [6] demonstrated the functionality of an all-solid-state battery with NaSICON solid electrolyte, which exhibits an ionic conductivity of 1.9×10^{-4} S cm^{-1} at 200 °C. The ionic conductivity

of the here-investigated NaSICON film annealed at 600 °C and post-treated at 200 °C is 3.6×10^{-4} S cm^{-1}, and hence, it is close to the reported value by Lalère et al.

The calculated activation energy of post-treated IDEs (in Fig. 7a) between 50 and 250 °C is shown in Fig. 7b. A slight increase in the activation energy E_a can be observed for samples annealed at 200 °C. Then, E_a decreases continuously with increasing annealing temperature of the samples. The NaSICON film annealed at 600 °C exhibits the lowest activation energy value of 0.48 eV (and the highest conductivity at room temperature). The reported activation energies of bulk materials in the literature are roughly 100–200 meV smaller than the E_a values of the NaSICON films produced via PAD.

One may object at this point that a full restoration of the conductivity has not yet been occurred, since the values of bulk samples have not been reached (according to the literature data, one finds 10^{-3}–10^{-4} S cm^{-1} at 50 °C for this composition [54]). For a comparison with literature with respect to the necessary annealing temperatures to achieve (almost) bulk values for the conductivity, the findings of Exner et al. [43] can be taken into account. These authors concluded that the reduced electrical conductivity that can be observed for all ceramic PAD films is due to internal strain in the as-deposited state.
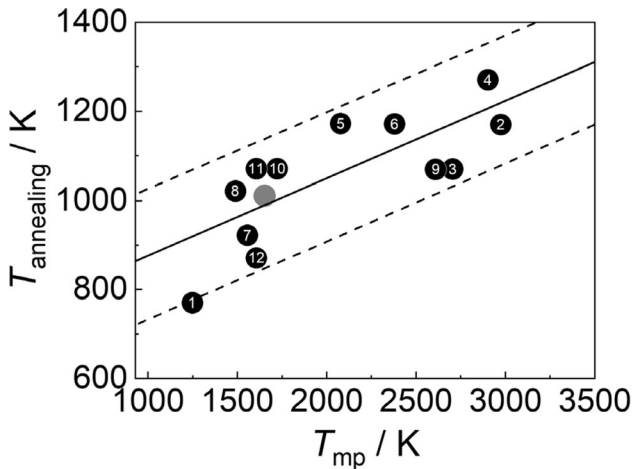
Figure 8 Required thermal annealing temperature $T_{annealing}$ for electrical conductive PAD films as a function of their melting point T_{mp} [43]. 1 = BiCuTiVOx [36], 2 = 8YSZ [18], 3 = GDC10 [57], 4 = BZY20 [45], 5 = BCY20 [45], 6 = BSY20 [45], 7 = LLZO [21], 8 = LAGP [58], 9 = STF35 [59], 10 = BFAT [60], 11 and 12 = NiMn$_2$O$_4$ [61, 62], gray filled dot = NaSICON (current work).

Depending on the melting temperature of the material, a thermal treatment with annealing temperatures ($T_{annealing}$) between 500 and 1000 °C is required for recovering the electrical properties of PAD films. Figure 8 shows the required annealing temperature for many materials, versus the corresponding melting point, T_{mp}, from [43]. Equation 3 is proposed to describe this trend within a scatter band of ± 150 K. The melting point T_{mp} of NaSICON depends on its composition [55]. However, the incongruent melting point T_{mp} of the composition Na$_3$Zr$_2$Si$_2$PO$_{12}$ used to produce NaSICON PAD films in this study, was reported to be 1300 °C [56]. This value (1573 K) is inserted as a filled gray dot in the Exner-plot in Fig. 8. According to Eq. 3, the required annealing temperature of NaSICON should be 992 K (720 °C). However, due to the scatter band of 150 K, the necessary restoration temperature may not have been reached. Nevertheless, the findings in this study agree with the overall picture as shown by Exner et al.

$$T_{annealing} = \frac{T_{mp}}{6} + 730K \tag{3}$$

From an all-solid-state battery perspective, two conclusions have to be drawn. First of all,

Na$_3$Zr$_2$Si$_2$PO$_{12}$ may not be appropriate, since one may need even prohibitively higher annealing temperatures, and/or the obtained conductivities may nevertheless be too low. Therefore, higher conductive compositions like sodium-excess [38], trivalent (La^{3+} [63], Y^{3+} [64]) or tetravalent (Ti^{4+} [65], Ce^{4+} [66]) ion substituted NaSICON should be studied in the future. In these compositions, conductivities in the range from $1. \times 10^{-4}$ S cm^{-1} to 1×10^{-3} S cm^{-1} may be reached at room temperature.

Conclusion

In the current study, we conducted initial work on the synthesis and fabrication of NaSICON solid electrolyte films via the PAD method followed by electrical characterizations of the produced films. NaSICON powders were synthesized by a solid-state synthesis method. PAD films of NaSICON are approximately 10 µm thick and highly dense with a crack-free microstructure. XRD and Rietveld refinement of the powder shows that the monoclinic NaSICON phase with only small amounts of ZrO$_2$ as an impurity phase was obtained. The phase composition is not affected by the PAD process.

By EIS, the electrical conductivity of the films was studied. In the as-deposited state, films exhibit a highly reduced conductivity in the range of 10^{-8}–10^{-7} S cm^{-1}. However, the low temperature conductivity increases by one order of magnitude with an annealing temperature above 300 °C. In summary, it can be stated that the powder aerosol deposition method could be promising for the fabrication of membranes for stationary all-solid-state-sodium batteries. As next steps, half and full cells will be built up utilizing this method. Additionally, other NaSICON-like compounds will be studied.

Acknowledgements

Author contributions

Funding

Data availability

The data presented in this study are available on request.

Declarations

Conflict of Interest The authors declare that they have no conflict of interests.

Ethical Approval Not applicable.

Supplementary Information: The online version contains supplementary material available at https://doi.org/10.1007/s10853-023-08642-w.

References

[1] Janek J, Zeier WG (2016) A solid future for battery development. Nat Energy. https://doi.org/10.1038/nenergy.2016.141

[2] Abraham KM (2015) Prospects and limits of energy storage in batteries. J Phys Chem Lett. https://doi.org/10.1021/jz5026273

[3] Abraham KM (2020) How comparable are sodium-ion batteries to lithium-ion counterparts? ACS Energy Lett. https://doi.org/10.1021/acsenergylett.0c02181

[4] Kim J-J, Yoon K, Park I, Kang K (2017) Progress in the development of sodium-ion solid electrolytes. Small Methods. https://doi.org/10.1002/smtd.201700219

[5] Hong H-P (1976) Crystal structures and crystal chemistry in the system $Na_{1+x}Zr_2Si_xP_{3-x}O_{12}$. Mater Res Bull. https://doi.org/10.1016/0025-5408(76)90073-8

[6] Lalère F, Leriche JB, Courty M, Boulineau S, Viallet V, Masquelier C, Seznec V (2014) An all-solid state NASICON sodium battery operating at 200 °C. J Power Sources. https://doi.org/10.1016/j.jpowsour.2013.09.051

[7] Akedo J (2006) Aerosol deposition of ceramic thick films at room temperature: densification mechanism of ceramic layers. J Am Ceram Soc. https://doi.org/10.1111/j.1551-2916.2006.01030.x

[8] Fan S-Q, Yang G-J, Li C-J, Liu G-J, Li C-X, Zhang L-Z (2006) Characterization of microstructure of Nano-TiO_2 coating deposited by vacuum cold spraying. J Therm Spray Tech. https://doi.org/10.1361/105996306X146901

[9] Kwon J, Park H, Lee I, Lee C (2014) Effect of gas flow rate on deposition behavior of Fe-based amorphous alloys in vacuum kinetic spray process. Surf Coat Technol. https://doi.org/10.1016/j.surfcoat.2014.10.026

[10] Akedo J (2008) Room temperature impact consolidation (RTIC) of fine ceramic powder by aerosol deposition method and applications to microdevices. J Therm Spray Technol. https://doi.org/10.1007/s11666-008-9163-7

[11] Kwon O-Y, Lee D-W, Oh J-M, Cai J, Kim B-S (2018) Characterization of broadband dielectric properties of aerosol-deposited Al_2O_3 thick films. J Ceram Process Res 19(4):290–295

[12] Park Y, Park D-S, Johnson SD, Yoon W-H, Hahn B-D, Choi J-J, Ryu J, Kim J-W, Park C (2017) Effect of gas flow rates and nozzle throat width on deposition of α-alumina films of granule spray in vacuum. J Eur Ceram Soc. https://doi.org/10.1016/j.jeurceramsoc.2017.02.021

[13] Schubert M, Exner J, Moos R (2014) Influence of carrier gas composition on the stress of Al_2O_3 coatings prepared by the aerosol deposition method. Materials. https://doi.org/10.3390/ma7085633

[14] Taira Y, Hatono H, Mizukane M, Tokita M, Atsuta M (2006) Effect of ceramic coating by aerosol deposition on abrasion resistance of a resin composite material. Dent Mater J 25(4):700–705

[15] Choi J-J, Choi J-H, Ryu J, Hahn B-D, Kim J-W, Ahn C-W, Yoon W-H, Park D-S (2012) Microstructural evolution of YSZ electrolyte aerosol-deposited on porous NiO-YSZ. J Eur Ceram Soc. https://doi.org/10.1016/j.jeurceramsoc.2012.04.024

[16] Choi J-J, Oh S-H, Noh H-S, Kim H-R, Son J-W, Park D-S, Choi J-H, Ryu J, Hahn B-D, Yoon W-H, Lee H-W (2011) Low temperature fabrication of nano-structured porous LSM–YSZ composite cathode film by aerosol deposition. J Alloys Compd. https://doi.org/10.1016/j.jallcom.2010.11.169

[17] Ryu HS, Lim TS, Ryu J, Hong S-H (2012) Corrosion protection performance of YSZ Coating on AA7075 aluminum alloy prepared by aerosol deposition. J Electrochem Soc. https://doi.org/10.1149/2.038302jes

[18] Exner J, Kita J, Moos R (2019) In- and through-plane conductivity of 8YSZ films produced at room temperature by aerosol deposition. J Mater Sci. https://doi.org/10.1007/s10853-019-03844-7

[19] Bredikhin SI, Agarkov DA, Agarkova E, Burmistrov I, Cherkasov A, Pukha V, Yalovenko D, Lyskov N (2019) Aerosol deposition as a promising technique to fabricating a thin-film solid electrolyte of solid oxide fuel cells. ECS Trans. https://doi.org/10.1149/09101.0403ecst

[20] Fuchita E, Tokizaki E, Ozawa E, Sakka Y (2010) Formation of zirconia films by aerosol gas deposition method using zirconia powder produced by break-down method. J Ceram Soc Jpn. https://doi.org/10.2109/jcersj2.118.948

[21] Hanft D, Exner J, Moos R (2017) Thick-films of garnet-type lithium ion conductor prepared by the Aerosol Deposition Method: the role of morphology and annealing treatment on the ionic conductivity. J Power Sources. https://doi.org/10.1016/j.jpowsour.2017.06.061

[22] Nazarenus T, Sun Y, Exner J, Kita J, Moos R (2021) Powder aerosol deposition as a method to produce garnet-type solid ceramic electrolytes: a study on electrochemical film properties and industrial applications. Energy Technol. https://doi.org/10.1002/ente.202100211

[23] Inada R, Okada T, Bando A, Tojo T, Sakurai Y (2017) Properties of garnet-type $Li_6La_3ZrTaO_{12}$ solid electrolyte films fabricated by aerosol deposition method. Prog Nat Sci Mater Int. https://doi.org/10.1016/j.pnsc.2017.06.002

[24] Inada R, Ishida K, Tojo M, Okada T, Tojo T, Sakurai Y (2015) Properties of aerosol deposited NASICON-type Li1.5Al0.5Ge1.5(PO4)3 solid electrolyte thin films. Ceram Int. https://doi.org/10.1016/j.ceramint.2015.05.062

[25] Kato T, Iwasaki S, Ishii Y, Motoyama M, West WC, Yamamoto Y, Iriyama Y (2016) Preparation of thick-film electrode-solid electrolyte composites on Li7La3Zr2O12 and their electrochemical properties. J Power Sources. https://doi.org/10.1016/j.jpowsour.2015.10.101

[26] Hanft D, Bektas M, Moos R (2018) Powder pre-treatment for aerosol deposition of tin dioxide coatings for gas sensors. Materials. https://doi.org/10.3390/ma11081342

[27] Bektas M, Hanft D, Schönauer-Kamin D, Stöcker T, Hagen G, Moos R (2014) Aerosol-deposited $BaFe_{0.7}Ta_{0.3}O_{3-\delta}$ for nitrogen monoxide and temperature-independent oxygen sensing. J Sens Sens Syst. https://doi.org/10.5194/jsss-3-223-2014

[28] Yang S, Kim H, Pawar RC, Ahn S-H, Lee CS (2015) Dielectric characteristics of a barium titanate film deposited by Nano Particle Deposition System (NPDS). Int J Precis Eng Manuf. https://doi.org/10.1007/s12541-015-0133-y

[29] Khansur NH, Eckstein U, Benker L, Deisinger U, Merle B, Webber KG (2018) Room temperature deposition of functional ceramic films on low-cost metal substrate. Ceram Int. https://doi.org/10.1016/j.ceramint.2018.06.027

[30] Kim E-S, Liang J-G, Wang C, Cho M-Y, Oh J-M, Kim N-Y (2019) Inter-digital capacitors with aerosol-deposited high-K dielectric layer for highest capacitance value in capacitive super-sensing applications. Sci Rep. https://doi.org/10.1038/s41598-018-37416-7

[31] Popovici D, Tsuda H, Akedo J (2009) Postdeposition annealing effect on $(Ba_{0.6},Sr_{0.4})TiO_3$ thick films deposited by aerosol deposition method. J Appl Phys. https://doi.org/10.1063/1.3086197

[32] Imanaka Y, Akedo J (2010) Embedded capacitor technology using aerosol deposition. Int J Appl Ceram Technol. https://doi.org/10.1111/j.1744-7402.2009.02359.x

[33] Sam Oh JA, Sun Q, Tian C, Song X, Chua B, Zeng K, Lu L (2022) Aerosol deposited freestanding $Na_3V_2(PO_4)_3$ thin film micro battery. Mater Today Energy. https://doi.org/10.1016/j.mtener.2022.101006

[34] Hanft D, Exner J, Schubert M, Stöcker T, Fuierer P, Moos R (2015) An overview of the aerosol deposition method: process fundamentals and new trends in materials applications. J Ceram Sci Technol. https://doi.org/10.4416/JCST2015-00018

[35] Schönauer D, Moos R (2010) Detection of water droplets on exhaust gas sensors. Sens Actuators B Chem. https://doi.org/10.1016/j.snb.2010.05.060

[36] Exner J, Fuierer P, Moos R (2014) Aerosol deposition of (Cu,Ti) substituted bismuth vanadate films. Thin Solid Films. https://doi.org/10.1016/j.tsf.2014.11.037

[37] Shu JH, Wikle HC, Chin BA (2010) Passive chemiresistor sensor based on iron (II) phthalocyanine thin films for

monitoring of nitrogen dioxide. Sens Actuators B. https://doi.org/10.1016/j.snb.2010.05.017

[38] Naqash S, Tietz F, Yazhenskikh E, Müller M, Guillon O (2019) Impact of sodium excess on electrical conductivity of $Na_3Zr_2Si_2PO_{12}$ + x Na_2O ceramics. Solid State Ionics. https://doi.org/10.1016/j.ssi.2019.03.017

[39] Narayanan S, Reid S, Butler S, Thangadurai V (2019) Sintering temperature, excess sodium, and phosphorous dependencies on morphology and ionic conductivity of NASICON $Na_3Zr_2Si_2PO_{12}$. Solid State Ionics. https://doi.org/10.1016/j.ssi.2018.12.003

[40] Exner J, Hahn M, Schubert M, Hanft D, Fuierer P, Moos R (2015) Powder requirements for aerosol deposition of alumina films. Adv Powder Technol. https://doi.org/10.1016/j.apt.2015.05.016

[41] Chun D-M, Ahn S-H (2011) Deposition mechanism of dry sprayed ceramic particles at room temperature using a nanoparticle deposition system. Acta Mater. https://doi.org/10.1016/j.actamat.2011.01.007

[42] Lee D-W, Kim H-J, Kim Y-H, Yun Y-H, Nam S-M (2011) Growth process of α-Al_2O_3 ceramic films on metal substrates fabricated at room temperature by aerosol deposition. J Am Ceram Soc. https://doi.org/10.1111/j.1551-2916.2011.04493.x

[43] Exner J, Nazarenus T, Hanft D, Kita J, Moos R (2020) What happens during thermal post-treatment of powder aerosol deposited functional ceramic films? explanations based on an experiment-enhanced literature survey. Adv Mater. https://doi.org/10.1002/adma.201908104

[44] Exner J, Schubert M, Hanft D, Kita J, Moos R (2019) How to treat powders for the room temperature aerosol deposition method to avoid porous, low strength ceramic films. J Eur Ceram Soc. https://doi.org/10.1016/j.jeurceramsoc.2018.08.008

[45] Exner J, Nazarenus T, Kita J, Moos R (2020) Dense Y-doped ion conducting perovskite films of $BaZrO_3$, $BaSnO_3$, and $BaCeO_3$ for SOFC applications produced by powder aerosol deposition at room temperature. Int J Hydrogen Energy. https://doi.org/10.1016/j.ijhydene.2020.01.164

[46] Murugan R, Thangadurai V, Weppner W (2007) Fast lithium ion conduction in garnet-type Li(7)La(3)Zr(2)O(12). Angew Chem (International ed. in English). https://doi.org/10.1002/anie.200701144

[47] Bohnke O, Ronchetti S, Mazza D (1999) Conductivity measurements on Nasicon and Nasicon-modified materials. Solid State Ionics. https://doi.org/10.1016/S0167-2738(99)00062-4

[48] Kim C-J, Chung J-K, Lim S-K, Rhee M-H (1996) Synthesis of solid electrolyte Nasicon by solid state reaction. Korean J Ceram 2(1):25–32

[49] Grady ZM, Tsuji K, Ndayishimiye A, Hwan-Seo J, Randall CA (2020) Densification of a solid-state NASICON sodium-ion electrolyte below 400 °C by cold sintering with a fused hydroxide solvent. ACS Appl Energy Mater. https://doi.org/10.1021/acsaem.0c00047

[50] Lunghammer S, Ma Q, Rettenwander D, Hanzu I, Tietz F, Wilkening H (2018) Bulk and grain-boundary ionic conductivity in sodium zirconophosphosilicate $Na_3Zr_2(SiO_4)_2PO_4$ (NASICON). Chem Phys Lett. https://doi.org/10.1016/j.cplett.2018.04.037

[51] Goodenough JB, Hong H-P, Kafalas JA (1976) Fast Na^+-ion transport in skeleton structures. Mater Res Bull. https://doi.org/10.1016/0025-5408(76)90077-5

[52] Bukun NG (1996) Superionic transitions in NASICON-type solid electrolytes. Ionics. https://doi.org/10.1007/BF02375870

[53] Guin M, Tietz F (2015) Survey of the transport properties of sodium superionic conductor materials for use in sodium batteries. J Power Sources. https://doi.org/10.1016/j.jpowsour.2014.09.137

[54] Park H, Jung K, Nezafati M, Kim C-S, Kang B (2016) Sodium ion diffusion in Nasicon ($Na_3Zr_2Si_2PO_{12}$) solid electrolytes: effects of excess sodium. ACS Appl Mater Interfaces. https://doi.org/10.1021/acsami.6b09992

[55] McEntire BJ, Bartlett RA, Miller GR, Gordon RS (1983) Effect of decomposition on the densification and properties of Nasicon ceramic electrolytes. J Am Ceram Soc. https://doi.org/10.1111/j.1151-2916.1983.tb10541.x

[56] Nicholas VA, Heyns AM, Kingon AI, Clark JB (1986) Reactions in the formation of $Na_3Zr_2Si_2PO_{12}$. J Mater Sci. https://doi.org/10.1007/BF00547935

[57] Exner J, Pöpke H, Fuchs F-M, Kita J, Moos R (2018) Annealing of Gadolinium-Doped Ceria (GDC) films produced by the aerosol deposition method. Materials. https://doi.org/10.3390/ma11112072

[58] Khan A, Ahn C-W, Ryu J, Yoon W-H, Hahn B-D, Choi J-J, Kim J-W, Park D-S (2014) Effect of annealing on properties of lithium aluminum germanium phosphate electrolyte thick films prepared by aerosol deposition. Met Mater Int. https://doi.org/10.1007/s12540-014-1018-9

[59] Exner J, Schubert M, Hanft D, Stöcker T, Fuierer P, Moos R (2016) Tuning of the electrical conductivity of Sr(Ti, Fe)$_O3$ oxygen sensing films by aerosol co-deposition with Al_2O_3. Sens Actuators, B Chem. https://doi.org/10.1016/j.snb.2016.02.033

[60] Murat Bektas—$BaFe_{(1-x)-0.01}Al_{0.01}Ta_xO_{3-\delta}$: A material for temperature independent resistive and thermoelectric oxygen sensors (2022). https://www.shaker.de/de/content/catalogue/index.asp?lang=de&ID=8&ISBN=978-3-8440-7459-8. Accessed 12 May 2022

[61] Ryu J, Park D-S, Schmidt R (2011) In-plane impedance spectroscopy in aerosol deposited $NiMn_2O_4$ negative temperature coefficient thermistor films. J Appl Phys. https://doi.org/10.1063/1:3592300

[62] Schubert M, Münch C, Schuurman S, Poulain V, Kita J, Moos R (2018) Characterization of nickel manganite NTC thermistor films prepared by aerosol deposition at room temperature. J Eur Ceram Soc. https://doi.org/10.1016/j.jeurceramsoc.2017.09.005

[63] Ruan Y, Song S, Liu J, Liu P, Cheng B, Song X, Battaglia V (2017) Improved structural stability and ionic conductivity of $Na_3Zr_2Si_2PO_{12}$ solid electrolyte by rare earth metal substitutions. Ceram Int. https://doi.org/10.1016/j.ceramint.2017.03.095

[64] Fuentes R (2001) Influence of microstructure on the electrical properties of NASICON materials. Solid State Ionics. https://doi.org/10.1016/S0167-2738(01)00701-9

[65] Chen D, Luo F, Zhou W, Zhu D (2018) Influence of Nb^{5+}, Ti^{4+}, Y^{3+} and Zn^{2+} doped $Na_3Zr_2Si_2PO_{12}$ solid electrolyte on its conductivity. J Alloy Compd. https://doi.org/10.1016/j.jallcom.2018.05.116

[66] Khakpour Z (2016) Influence of M: Ce^{4+}, Gd^{3+} and Yb^{3+} substituted $Na_{3+x}Zr_{2-x}M_xSi_2PO_{12}$ solid NASICON electrolytes on sintering, microstructure and conductivity. Electrochim Acta. https://doi.org/10.1016/j.electacta.2016.02.199